Journal of Materials Chemistry A

Understanding Additive Controlled Lithium Morphology in Lithium Metal Batteries

Journal:	*Journal of Materials Chemistry A*
Manuscript ID	TA-ART-06-2020-006020.R1
Article Type:	Paper
Date Submitted by the Author:	28-Jul-2020
Complete List of Authors:	Kasse, Robert; Stanford University, Department of Materials Science and Engineering Geise, Natalie; Stanford University, Department of Chemistry Ko, Jesse; SLAC National Accelerator Laboratory, Stanford Synchrotron Radiation Lightsource; Johns Hopkins University Applied Physics Laboratory, Research and Exploratory Development Nelson Weker, Johanna; SLAC National Accelerator Laboratory, Stanford Synchrotron Radiation Lightsource Steinrück, Hans-Georg; SLAC National Accelerator Laboratory, Stanford Synchrotron Radiation Lightsource; Universität Paderborn, Department Chemie Toney, Michael; SLAC National Accelerator Laboratory, Stanford Synchrotron Radiation Lightsource

SCHOLARONE™
Manuscripts

Understanding Additive Controlled Lithium Morphology in Lithium Metal Batteries

Robert M. Kasse[a], Natalie R. Geise[b], Jesse S. Ko[c, d], Johanna Nelson Weker[c], Hans-Georg Steinrück[c, e], Michael F. Toney[c]

[a] Stanford University, Department of Materials Science and Engineering, Stanford, CA, USA
[b] Stanford University, Department of Chemistry, Stanford, CA, USA
[c] SLAC National Accelerator Laboratory, Stanford Synchrotron Radiation Lightsource, Menlo Park, CA, USA
[d] Johns Hopkins University Applied Physics Laboratory, Research and Exploratory Development, Laurel, MD, USA
[e] Department Chemie, Universität Paderborn, Paderborn, Germany

Abstract

Directing the morphology of lithium metal deposits during electrodeposition is crucial to the development of safe, high energy density batteries with long cycle life. Towards this end, mechanistic insight is imperative to understand the impact of electrolyte components and cycling conditions on lithium morphologies. In this work, we used a standard carbonate-based electrolyte while systematically adding water (0-250 ppm, corresponding to 0-500 ppm HF) in Li||Cu cells to study the links between electrolyte composition, initial solid electrolyte interphase (SEI) formation, and morphology of electroplated lithium metal using electrochemical characterization, X-ray scattering, X-ray photoelectron spectroscopy, and electron microscopy. Under conditions in which the electrolyte contains several hundred ppm added HF and applied constant currents on the order of 0.5 mA/cm^2, this system yields electrodeposited lithium metal with a highly monodispersed columnar morphology. Systematic experimental investigation of the HF reduction process, nature of the initial SEI, and the structure of the electrodeposited lithium metal enable insights to be drawn concerning the underlying mechanisms of columnar lithium formation. This morphology arises from an SEI layer comprising crystalline LiF deposits on the copper current collector surface, formed through selective reduction of HF at high potential, embedded in an amorphous matrix of solvent reduction products. This interphase structure contains fast lithium-ion diffusion pathways which lead to a high nucleation density and uniform growth of lithium metal deposits. The mechanism proposed herein will help to inform future electrolyte additive design and formation cycling protocols for lithium metal batteries.

Introduction

In recent years, scientists have referred to lithium metal as the "Holy Grail" of battery anodes due to its low electrode potential (-3.04 V vs SHE), low density (0.54 g/mL), and high specific capacity (3,860 mAh/g).[1–5] These properties make lithium an attractive candidate to replace graphite anodes (-2.94 V vs SHE, 2.2 g/mL, 370 mAh/g) used in conventional lithium-ion batteries with applications ranging from portable electronics to electric vehicles, and lithium metal anodes can enable next generation battery chemistries such as lithium-sulfur and lithium-air.[6–8] There are, however, challenges hindering commercialization of lithium metal anodes and several issues remain to be resolved with regards to the poor safety and low cycle life of current lithium metal batteries. Ultimately these issues stem from poor control over lithium morphology

during plating and stripping processes at the anode surface, leading to high surface area deposits (e.g. whiskers, mossy microstructure) which rapidly react with and consume electrolyte.[9–11] Furthermore, there is potential to form dendrites which can cause an internal short circuit and cell overheating.[9,12]

Various approaches have been employed to address these issues through the engineering of *ex situ* deposited surface coatings, solid electrolyte interphase (SEI) transplantation, electrolyte additives, and 3D host materials.[13–16] These studies have been largely empirical with limited effort directed towards a fundamental understanding of the interplay between electrolyte composition, SEI formation, and lithium metal morphology. For example, it is important to quantify the amount of lithium lost into the SEI, soluble reduction products, "dead" lithium, and corrosion, and to identify how these loss mechanisms are mitigated by using additives or surface coatings. This knowledge will enable the development of commercially viable solutions.[17] Empirical approaches have had some success in improving Coulombic efficiency and cycle life, but in most cases it is unclear which loss mechanism is mitigated and how. We consider understanding these processes mechanistically to be the "Holy Grail" of lithium anode research, knowledge that may be extensible to other battery chemistries.

Several literature reports have described the growth of lithium metal with a columnar geometry with only ppm level concentrations of water as an electrolyte additive on copper, brass, nickel, and stainless steel working electrodes.[18–21] Over the course of 48-72 hours most of the added water reacts with PF^-_6 anions to form HF (Reaction 1).[22] Strmcnik *et al.* reported that upon lowering the potential of the working electrode, HF is electrocatalytically reduced on the surface to form LiF (Reaction 2)[23], and it is this layer of reaction products that is believed to be responsible for directing the lithium deposit morphology.[19] We note that LiF can also be formed via the direct reduction of PF_6^-, however, this is predicted to occur at lower voltages.[24,25] Other groups have also reported columnar lithium metal growth using other electrolyte additives[26,27] (e.g. $CsPF_6$, $LiAsF_6$) or *ex situ* deposited LiF layers.[28] However, there is still a lack of understanding for the correlation between the presence of LiF in the initial SEI and the resulting columnar growth, and an optimum additive concentration has not been explained. Furthermore, LiF is an SEI component in almost all lithium-based batteries which contain a fluorinated salt, solvent, or additive in the electrolyte, yet columnar lithium metal is unique to a few systems, thus its presence alone is not sufficient to produce any particular microstructure.

$$H_2O + LiPF_6 \rightarrow 2\ HF + LiF + POF_3 \quad (1)$$

$$HF + Li^+ + e^- \rightarrow LiF + \tfrac{1}{2}\ H_2 \quad (2)$$

Due to the sensitivity of lithium deposit size and shape to small composition changes in electrolytes such as 1 M $LiPF_6$ in EC/DMC with 0-500 ppm added HF, we have chosen to use this system in our case study. In this work, we used a combination of electrochemical characterization, electron microscopy, X-ray photoelectron spectroscopy (XPS), and *operando* synchrotron X-ray scattering to determine the key SEI and electrolyte properties which direct the evolution of a columnar lithium metal morphology in "anode-free" Li||Cu cells.[29,30] We report this SEI layer is composed of crystalline LiF deposits on the copper current collector surface,

formed through selective reduction of HF at ~2 V vs Li/Li^+, embedded in an amorphous matrix of solvent reduction products. This interphase structure contains fast lithium-ion diffusion pathways which lead to a high nucleation density and uniform growth of lithium metal deposits. Our proposed mechanisms will help to inform future electrolyte additive selection and rational cycling protocols for high energy density lithium metal batteries.

Experimental

Electrolyte Preparation

From 1 M $LiPF_6$ in EC/DMC (LP30, Gotion), a stock solution was prepared by using a micropipette to add a controlled amount of Milli-Q water, which when fully reacted (48-72 hours) with the $LiPF_6$ adds 770 ppm of HF to the solution. The stock solution was then diluted with as-received LP30 to make solutions with 10, 100, and 500 ppm added HF. Solutions were stored in high density polyethylene bottles inside of optically opaque aluminized polymer bags in a UHP argon glovebox to protect against photodegradation and prevent SiO_2 etching which would occur if glass vials were used.

Working Electrode Preparation

Copper evaporated onto a glass slide was used as the working electrode. The copper films exhibit strong (111) crystallographic texture, as is common for face centered cubic metals. Glass slides were cut to size, ultrasonicated in acetone, scrubbed with soapy water (Liquinox), rinsed with deionized water, and dried with a nitrogen gun prior to evaporation. A KJL electron-beam evaporator was used to deposit 200 nm of copper with a 5 nm titanium adhesion layer and the slides were then stored in an argon glovebox.

Prior to cell assembly the working electrode was removed from the glovebox for acid cleaning to remove the native oxide. The electrode was first cleaned with a 1 M aqueous sulfuric acid solution for one minute, thoroughly rinsed with Milli-Q water, followed by a rinse with ethanol, and rapidly transferred to the antechamber of a UHP argon glovebox while still damp with ethanol and vacuum dried for 15 minutes. See the Electronic Supplementary Information for a discussion on the effects of this cleaning procedure on SEI formation and lithium metal plating.

Electrochemical Measurements

All electrochemistry experiments were performed using a Bio-Logic potentiostat and EC-Lab software in a two-electrode configuration with an evaporated copper working electrode (detailed above) and a 750 μm lithium foil counter/reference electrode (Alfa Aesar). The electrochemical cell used was a PTFE "cone-cell" design fabricated in house, with an electrode spacing ~10 mm, which eliminates all conductive surfaces aside from the well-defined working electrode active area, resulting in near-zero side current.[31] Galvanostatic cycling was performed at current densities (0.2-1.0 mA/cm^2) well below the limiting current density for the cell, calculated using the Sand's time equations.[32]

Operando X-ray Scattering Cell

To allow for X-rays to probe the surface of the copper working electrode during electrochemical cycling, a cell (similar to that used in references [33,34]) with X-ray transparent windows was designed for *operando* experiments at the beamline (Figure 1). PTFE-coated stainless-steel current collector screws (with the PTFE removed from the bottom) are placed outside of the electrolyte reservoir to minimize side reactions. The lithium foil is positioned to be out of the X-ray beam so only the copper surface is probed. The electrode spacing is ~5 mm and the working electrode active area is 1.08 cm^2. Note that the electrode spacing required for X-ray access to the surface necessitates an open cell design with no applied pressure, as would be found in a coin or pouch cell geometry. Fluorosilicone gaskets and X-ray transparent Kapton windows seal the cell on both sides, and the entire cell is placed in a sealed chamber while still in a glovebox for transport to the beamline. Helium is flowed through the chamber during experiments to minimize air scattering and prevent any air or moisture exposure.

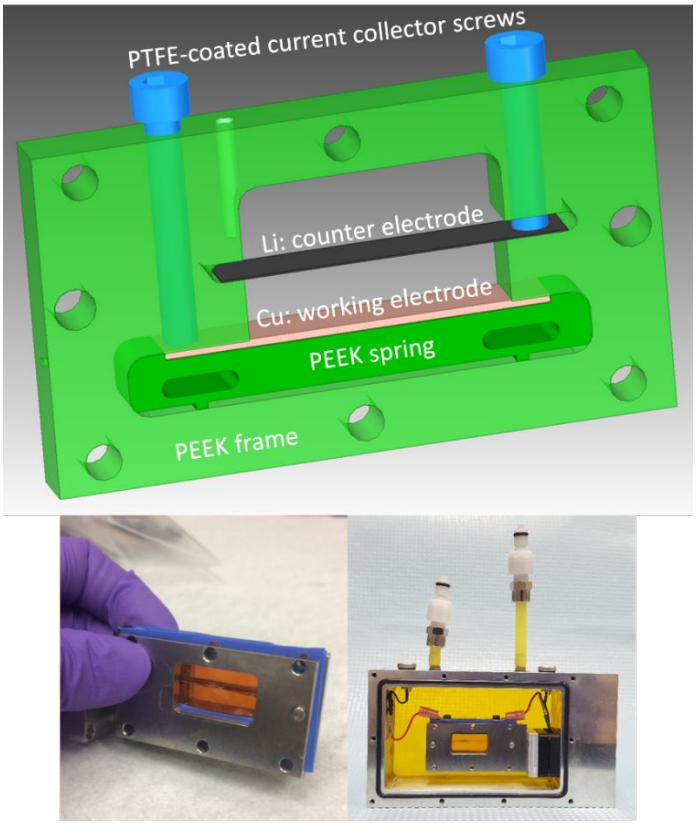

Figure 1: (top) Rendering of the operando X-ray cell showing the copper working electrode, lithium counter electrode, and PTFE-coated stainless steel current collector screws. (bottom left) Photograph of the operando X-ray cell. (bottom right) Photograph of the operando X-ray cell inside of a chamber which contains a flow of helium gas during scattering experiments.

Grazing Incidence Wide Angle X-ray Scattering

Grazing incidence wide angle X-ray scattering (GIWAXS) experiments were performed at beamline 11-3 of the Stanford Synchrotron Radiation Lightsource (SSRL) at SLAC National Accelerator Laboratory. The incident photon energy was 12.7 keV (λ = 0.976 Å) with a sample

to detector distance of ~210 mm, calibrated using a LaB_6 standard. Each 2D image was acquired for 120 seconds. Grazing incidence X-ray scattering data was reduced and analyzed using in-house Python scripts employing the PyFAI and pygix libraries.[35,36]

Grazing Incidence Small Angle X-ray Scattering

Grazing incidence small angle X-ray scattering (GISAXS) experiments were performed at SSRL beamline 1-5. The incident photon energy was 14.0 keV (λ = 0.886 Å) with a sample to detector distance of ~2.8 m, calibrated using a silver behenate standard. Each 2D image was acquired for 8 seconds. PyFAI and pygix libraries[35,36] were used for data reduction and analysis.

X-ray Photoelectron Spectroscopy

XPS experiments were performed at the Stanford Nano Shared Facility (SNSF) using a PHI Versaprobe 1 Scanning XPS Microprobe. The X-ray source was Al K-alpha (1486.6 eV). The pass energy was set to 23.5 eV. Both ion beam and electron beam charge neutralization were used. Remaining peak shifts due to surface charging were corrected by normalizing to the C 1s peak at 284.8 eV. XPS fitting was performed using the PHI MultiPak software package. Sputtering was performed using an argon ion source with a nominal sputtering rate of 2 nm/min calibrated using SiO_2.

Scanning Electron Microscopy

Scanning electron microscopy (SEM) images were acquired using an FEI Quanta FEG 250 scanning electron microscope. The accelerating voltage was 10 kV and the working distance was 10 mm. Samples were transported to the SEM in a heat-sealed aluminized polymer bag filled with UHP argon. Air exposure during transfer from the bag to the microscope was less than 5 seconds.

Results & Discussion

The addition of ppm levels of HF to lithium metal battery electrolytes causes a dramatic difference in the morphology of electrodeposits and a signature of HF reduction can easily be identified in electrochemistry data. While the galvanostatic plating curve for as-received electrolyte has a sloping shape with no pronounced voltage plateau until that corresponding to solvent reduction[25,37] at ~0.5 V vs Li/Li^+ (Figure 2a), the curve for electrolyte with 100 ppm added HF (Figure 2b) exhibits a clear voltage plateau at ~2.0 V vs Li/Li^+, corresponding to electrocatalytic reduction of HF (Reaction 2). The morphology of lithium metal deposited from each electrolyte can be seen in the SEM images, which show a mossy microstructure formed in as-received electrolyte (Figure 2c) and a smooth columnar morphology when 100 ppm added HF is present (Figure 2d).

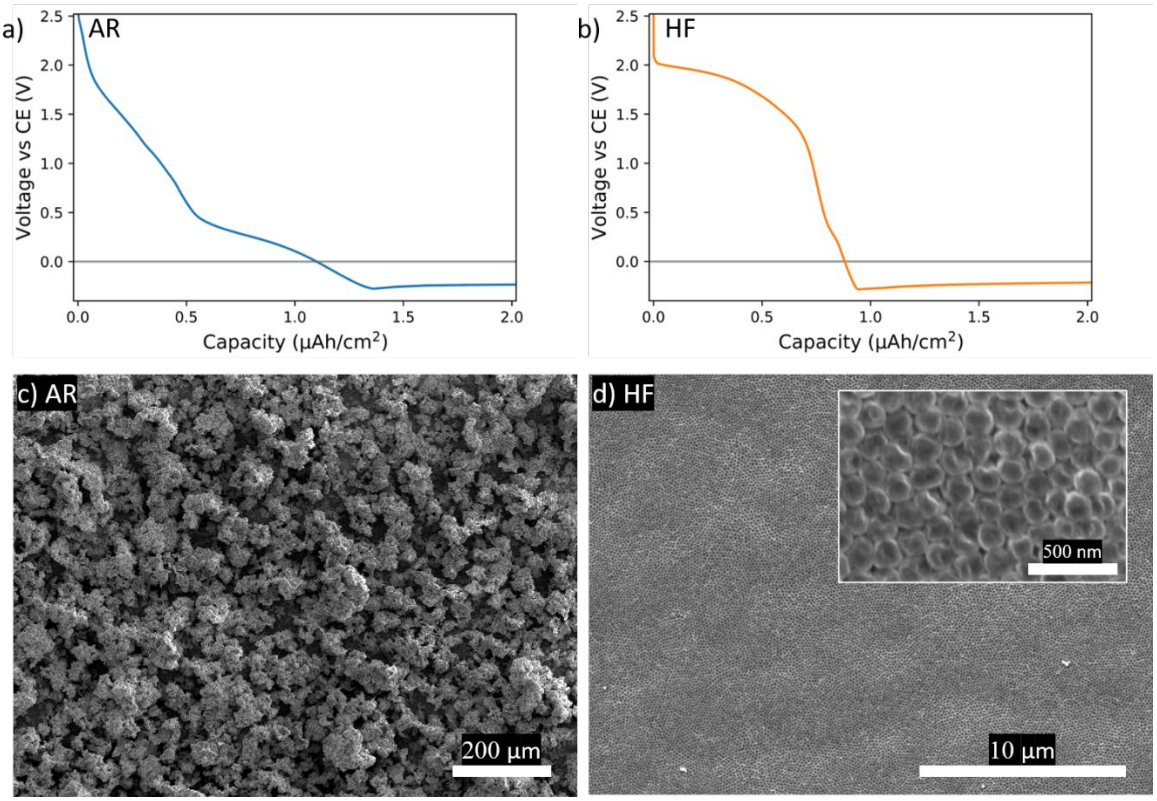

Figure 2: Capacity vs. voltage curves from galvanostatic electroplating of 1 mAh/cm² lithium metal at 0.5 mA/cm² in 1 M $LiPF_6$ in EC/DMC (a) as-received (AR) and with (b)100 ppm added HF. Top-view SEM images of the resulting lithium metal morphology in (c) as-received electrolyte and that with (d) 100 ppm added HF. Note the different scale bars in (c) and (d) were chosen to highlight relevant features of the two morphologies.

Experimental results providing insight into the stepwise, mechanistic relationship between the presence of added HF in the electrolyte, initial SEI formation on a copper working electrode, and ultimately the effects on morphology of electroplated lithium metal will be presented and discussed in subsequent subsections. The results are presented in the order in which the processes would occur during galvanostatic deposition of lithium metal, i.e. bare copper, SEI coated copper, and lithium plating. In the final subsection, a mechanism is proposed to explain the phenomenon of columnar lithium metal growth, tying together all the experimental results, and demonstrating the interrelation between electrolyte composition, initial SEI formation, and morphology of plated lithium metal.

Initial SEI Directs Columnar Growth

Electrolyte additives may modify lithium deposition in several different ways, e.g. by influencing initial SEI formation on the current collector, the nucleation stage of lithium metal deposition, the growth of lithium metal deposits, or some combination thereof.[38] To investigate during which step of lithium metal electrodeposition HF plays an active role, a cell was first galvanostatically brought down to 0 V vs the counter electrode (CE, Li/Li^+) at 0.5 mA/cm² in LP30 containing 100 ppm added HF to form the initial SEI on copper (Figure 3a). The

electrolyte was then removed, the cell rinsed with as-received LP30, and refilled with as-received LP30 for deposition of lithium metal (Figure 3b). There is no voltage plateau ~2V indicative of HF reduction, but we observe and additional small amount of capacity below 1 V which is consistent with solvent reduction.[37,39] Lithium metal with a highly monodispersed columnar morphology (Figure 3c) was still deposited although there was no HF in the electrolyte during electroplating. This demonstrates that it is the initial SEI on copper which directs the microstructure and that HF does not play an active role beyond the initial SEI formation. This experimental evidence is in agreement with studies in the literature that report the formation of a columnar microstructure without additives when a LiF rich layer was deposited *ex situ* on copper prior to cell assembly.[20,28]

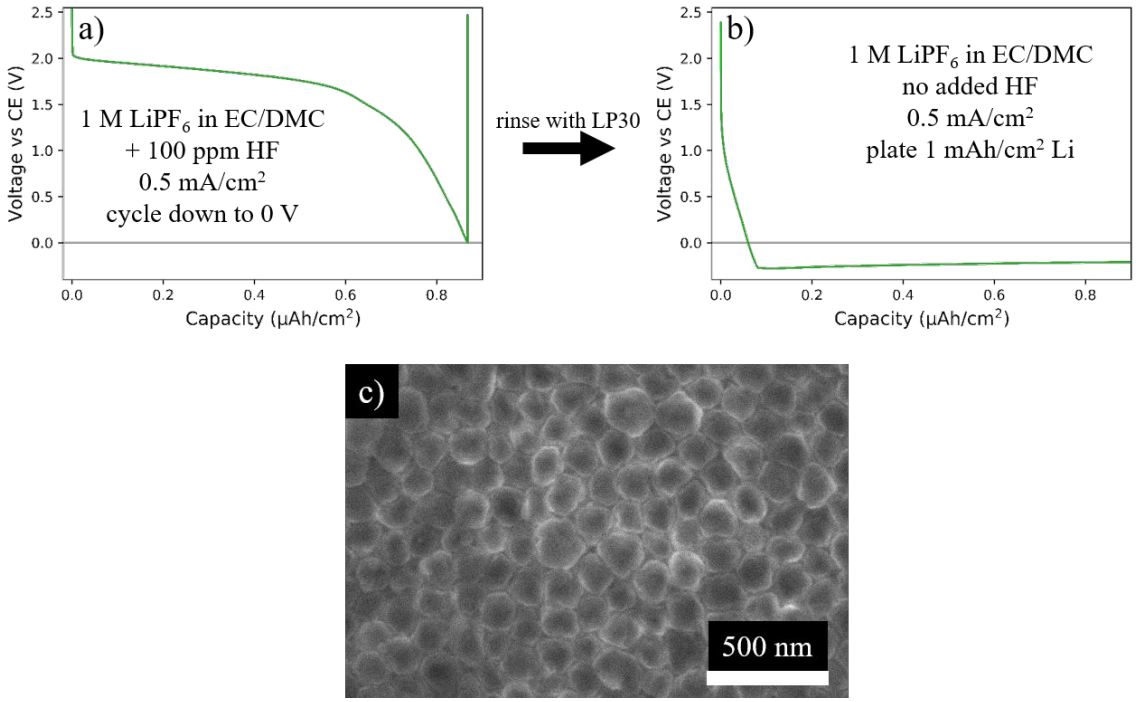

Figure 3: (a) Capacity vs voltage plot during formation of the initial SEI on copper galvanostatically brought to 0 V at 0.5 mA/cm² in LP30 +100 ppm HF. (b) Capacity vs voltage plot for electroplating of lithium metal at 0.5 mA/cm² in LP30 without added HF after initial SEI formation and rinsing. (c) Top-view SEM micrograph showing columnar morphology directed by the initial SEI.

As the initial SEI formed on copper modifies the nucleation and growth of lithium metal in a way that gives rise to a columnar microstructure, understanding the formation of this layer and its resulting properties is imperative. XPS results show that the initial SEI formed by galvanostatically bringing copper working electrodes to 0 V vs Li/Li^+ at 0.5 mA/cm² in LP30 electrolyte with and without added HF are quite similar in chemical composition (Table S1). Both SEIs contain primarily LiF, LiOH, and organic species (Figure 4), indicating that the nanostructure of this layer rather than its chemistry is likely key to modifying lithium nucleation and growth. The thickness of this initial SEI layer is roughly 2-3 nm based both on the charge passed (~3 nm, assuming fully dense and uniform LiF (Figure 3a)) and the Ar ion sputter rate (~2 nm, calibrated using SiO_2, Figure S3). The presence of a smaller peak around 687.6 eV in

the F1s spectrum for the as-received sample in Figure 4a corresponds to PF^-_6 and could be due to a more porous SEI that traps electrolyte. This is another indication of different SEI structures with and without an HF additive. Alternatively, this could be residue from incomplete electrolyte removal during rinsing.

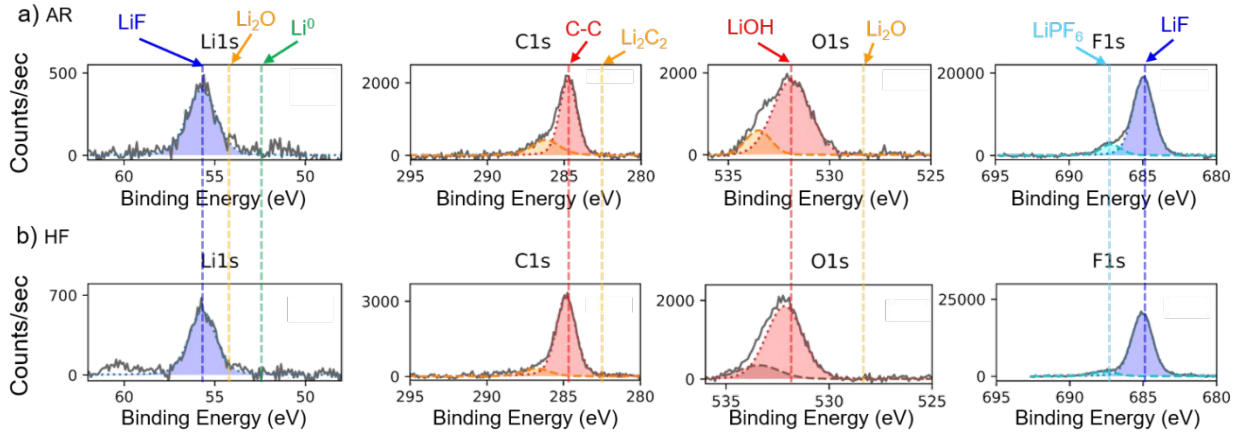

Figure 4: (a) XPS surface spectra of SEI on copper in as-received (AR) LP30. (b) XPS surface spectra of SEI on copper in LP30 with 100 ppm added HF. Samples were galvanostatically brought to 0 V at 0.5 mA/cm^2.

Directing the LiF Content of the Initial SEI

To study the electrolyte reduction processes resulting in SEI formation, cyclic voltammetry (CV) was performed systematically as a function of added HF concentration (as-received, +10, +100, and +500 ppm) and voltage sweep rate. Figure 5 shows a series of CV scans measured at 5 mV/s in electrolytes with varying concentrations of HF. The peak at ~2 V, indicated by the dashed line, results from the electrocatalytic reduction of HF to form LiF (Reaction 2). The additional peak at higher potential in the as-received electrolyte may be attributed to either PF^-_6 or POF_3 reduction.[25,40] The slight shift in peak position to higher potentials (from 1.9 to 2 V) with increasing HF concentration is consistent with the report by Strmcnik *et al*.[23] Solutions with more HF exhibit higher peak currents and increased capacity going into SEI formation. If a uniform film of LiF alone were fully passivating the copper surface, this would be achieved at a specific capacity as further HF reduction would be prevented by the passivation, and increased HF in the electrolyte would not lead to increased SEI capacity.[23] However, this data suggests that LiF alone does not passivate the copper surface at these HF concentrations and scan rates because increased HF concentration in the electrolyte results in a corresponding increase in the capacity of the HF reduction peak. Passivating LiF films can be formed under different conditions, however, namely at slower scan rates and on smoother single-crystalline substrates.[41] We rationalize that HF reduction is limited by the availability of HF at this interface, which in turn determines the amount of LiF that is formed in the initial SEI.

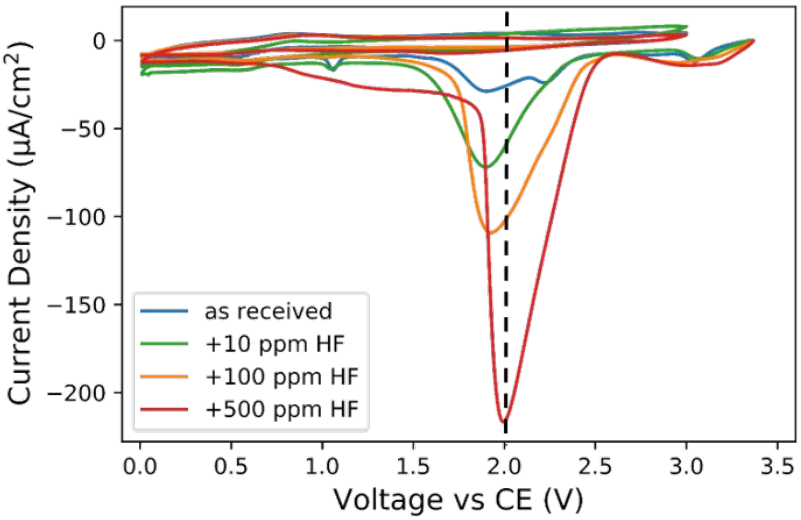

Figure 5: Cyclic voltammetry scans on copper in LP30 electrolytes with different concentrations of added HF. The sweep rate for all scans was 5 mV/s. The dashed line indicates the HF reduction peak.

Voltammetric scans of LP30 with 100 ppm added HF were collected at a series of sweep rates covering four orders of magnitude (0.5 – 500 mV/s) to determine which step of the SEI formation process is rate limiting. The background subtracted peak currents from the raw data (Figure 6a) were fit to the equation $\log(i_{max}) = \log(a \cdot v^b)$, where i_{max} is the peak current density at the HF reduction potential, v is the CV sweep rate, and a and b are constants. The fit of those data to the equation (Figure 6b) yields a line with a slope of $b = 0.494 \pm 0.007$, which is indicative of a diffusion limited process.[32] This ½ power law behavior is the diffusion-limited response of HF to the copper surface, since copper does not appreciably alloy or intercalate lithium, which is a key advantage of using this analysis for this system. This conclusion is consistent with the results of rotating disc electrode experiments in literature.[23,42] A slower CV scan provides sufficient time for HF to diffuse from the bulk electrolyte to the copper surface and be reduced to form LiF (Reaction 2). This is shown in Figure 7 for both slower scan rates in voltammetry (Figure 7a) and lower current densities during galvanostatic experiments (Figure 7b), which result in increased capacity at positive potentials from HF reduction. The data shown in Figure 7a was obtained by normalizing the raw CV data shown in Figure 6a by scan rate to yield capacity-voltage plots, which are more easily compared to galvanostatic cycling data. A longer voltage plateau in these capacity-voltage plots indicates the reduction of more HF. A potentiostatic hold at the HF reduction potential ~ 1.9 V was also performed for 12 hours, after which the current density was <0.5μA/cm^2, as shown in Figure 7b, with the reduction capacity at this potential being very similar to that of the slowest galvanostatic measurement taken at 0.005 mA/cm^2. The amount of charge passed, and thus LiF in the initial SEI, can be controlled by carefully choosing an optimal concentration of HF in the electrolyte and appropriate rate of electrochemical cycling, allowing for precise tuning of SEI properties.

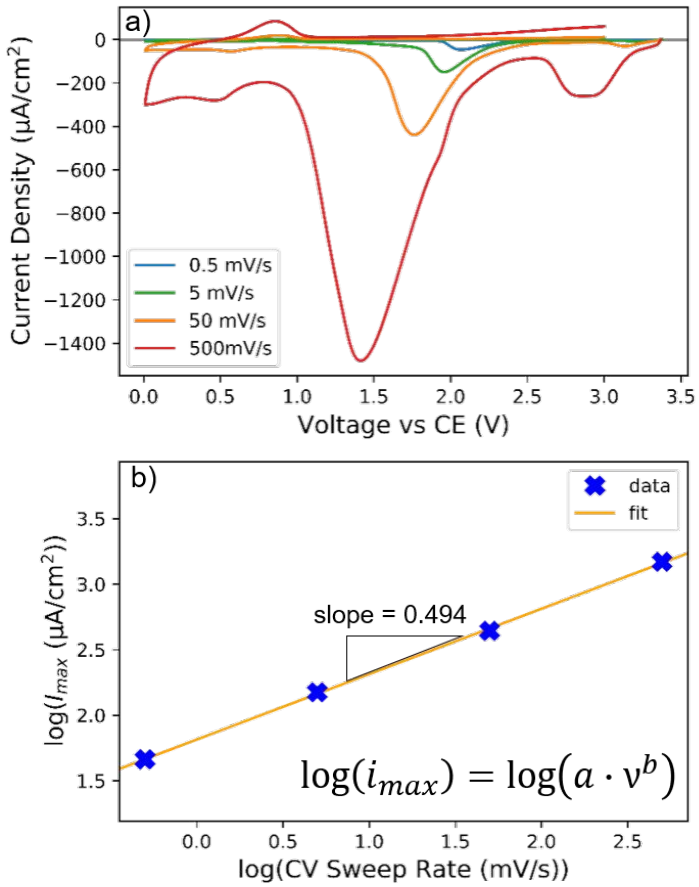

Figure 6: (a) Cyclic voltammetry scans on copper collected using several different voltage sweep rates in LP30 electrolyte with 100 ppm added HF. (b) Plot of log(sweep rate) vs log(i_{max}) showing the HF reduction process is limited by diffusion of HF to the copper surface as indicated by the fit of the data to the equation shown, yielding a slope of b = 0.494±0.007.

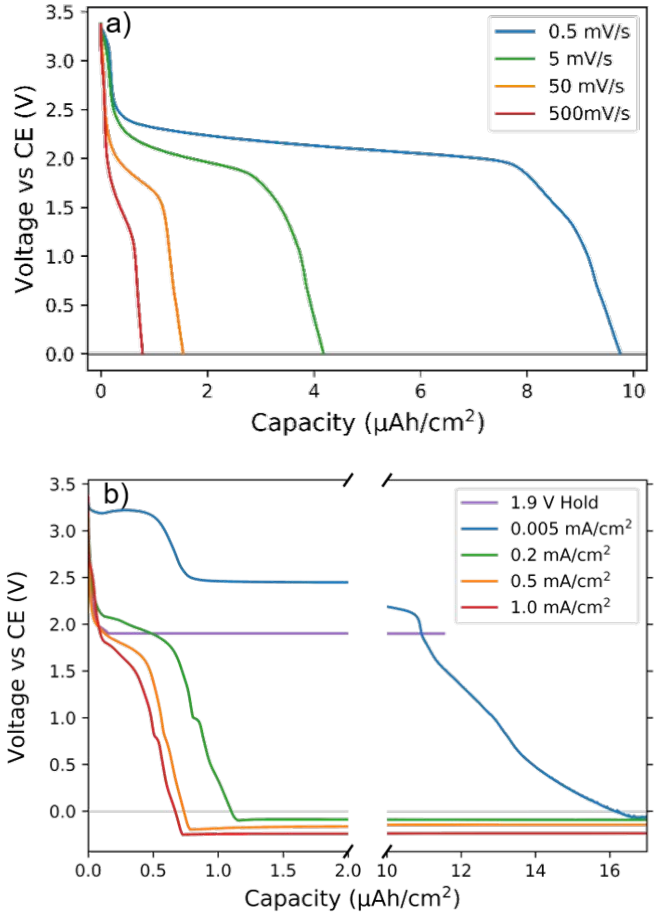

Figure 7: Capacity vs voltage plots from (a) cyclic voltammetry and (b) constant current cycling tests. All cells used LP30 with 100 ppm added HF. The plot in (a) was obtained by normalizing CV data by scan rate to obtain differential capacities at each potential and plotted with the same axes as the galvanostatic data shown in (b). Note the presence of a small second plateau in the galvanostatic data at ~0.7-0.9 V vs Li/Li$^+$, consistent with carbonate solvent reduction.

In situ GIWAXS was used to probe the crystallinity and crystallographic texture of the initial SEI layer formed on copper in 100 ppm added HF electrolyte. The initial SEI, formed by galvanostatically bringing the potential down to 0 V vs Li/Li$^+$ by cycling at 0.5 mA/cm^2, was found to contain crystalline LiF particles as evidenced by the small broad peak at 2.71 Å^{-1} in the inset of Figure 8a, corresponding to the (111) crystallographic plane. These LiF crystallites exhibit (111) texturing as shown by the peaks at ±70.5° in the I(χ) analysis (Figure 8b and Figure S5), which is reasonable given the face centered cubic rock salt structure of LiF. Scherrer analysis of the LiF (111) peak width from the I(q) data indicates a crystallite size on the order of ~5 nm, slightly larger than the SEI thickness calculated from both charged passed and XPS depth profiling, suggesting LiF does not form a continuous film. The other SEI components are either amorphous or too thin to characterize with GIWAXS. No crystallographic texture is evident in the SEI formed on copper from an electrolyte without added HF (Figure S4). The texturing may only occur in electrolyte with added HF because LiF is formed at higher potential vs Li/Li$^+$ due

to selective HF reduction, and LiF is the only solid product of this reaction. Therefore, the reduction process does not have to compete for reactants (lithium ions, fluorine atoms, electrons) or physical space on the copper surface, resulting in more facile LiF deposition homogenously distributed across the working electrode. In the case without HF, multiple reduction processes (e.g. PF^-_6, solvent) which yield multiple solid products (e.g. LiF, Li_2O, Li_2CO_3, organic species) all occur simultaneously at the applied scan rates, resulting in more random LiF formation.

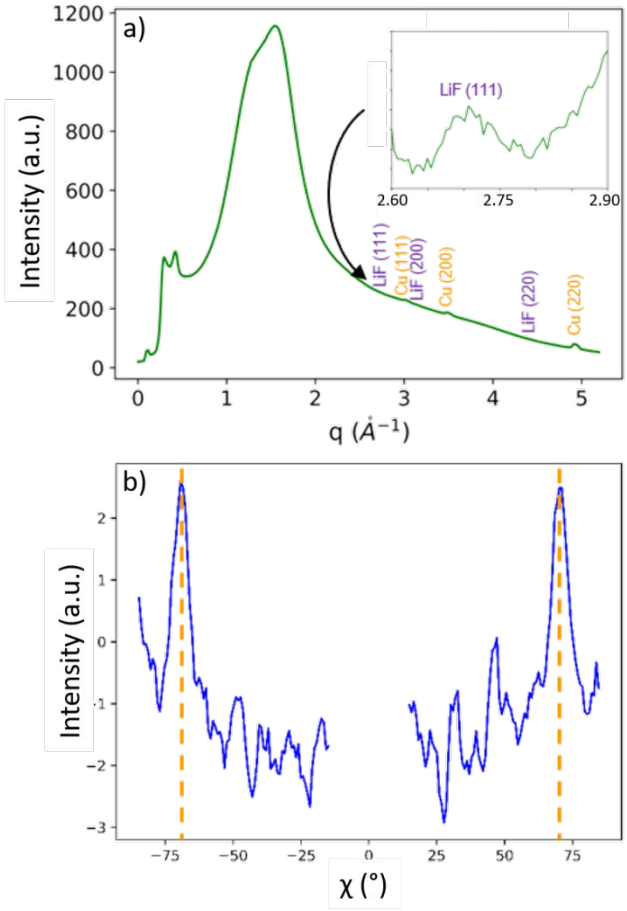

Figure 8: (a) 1D scattering pattern of SEI formed on copper by galvanostatic cycling at 0.5 mA/cm² down to 0 V vs Li/Li⁺ in LP30 with 100 ppm added HF. The large broad peak around 1.5 Å⁻¹ is due to amorphous scattering from the liquid electrolyte and glass substrate. Inset shows a zoom in of the LiF (111) peak after background subtraction. (b) I(χ) at the LiF (111) diffraction peak showing peaks at ± 70.5° (dashed lines) indicative of (111) texturing. The data was background subtracted using the average of I(χ) at ±0.1 Å⁻¹ above/below the LiF (111) peak as the background.

Mechanism of Copper Passivation and SEI Nanostructuring

We showed above that LiF formation slows significantly after HF is depleted near the copper surface. We further conclude that solvent reduction follows in between and/or on top of LiF particles. This is evidenced by a much shorter second plateau at ~0.7-0.9 V vs Li/Li⁺ (Figure 7b) and is consistent with experimental carbonate solvent reduction potentials from literature.[37,39] When the remaining unpassivated areas of the electrode surface become covered

with solvent reduction products, further electrolyte reduction is significantly slowed, as evidenced by the much reduced peak current in subsequent CV sweeps (Figure 5)

To test this hypothesis, HF was used as a probe of unpassivated surface area by first cycling a cell down to 1.5 V vs Li/Li^+ such that HF becomes depleted near the copper surface but solvent has not yet been reduced. The HF depletion layer was then removed by lightly agitating the solution with bubbles created using a pipette, and the cell was again galvanostatically brought down to 0 V vs Li/Li^+ (Figure 9). The presence of a second HF reduction plateau at the same potential indicates there is working electrode surface available for further reaction and that the plateau in the first half cycle ended due to HF depletion rather than electrode passivation by LiF. The same behavior is observed if, instead of light agitation with a pipette, the cell is rested for several hours before applying current a second time.

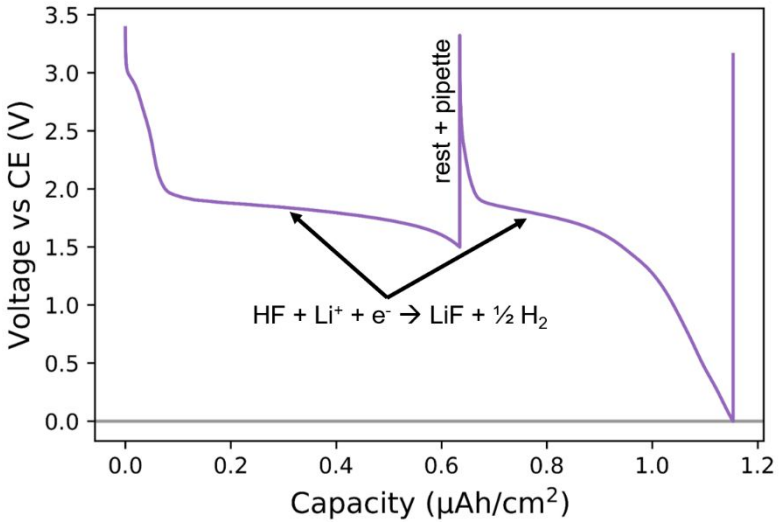

Figure 9: Capacity vs voltage plot of a cell containing LP30 with 100 ppm added HF first galvanostatically brought down to 1.5 V vs Li/Li^+ at 0.5 mA/cm^2, indicating HF is depleted near the copper surface, then down to 0 V vs Li/Li^+ after the depletion layer is removed by light agitation with a pipette. The voltage plateau during the second half cycle at the HF reduction potential shows there is unreacted copper available and that the plateau in the first half cycle ended due to HF depletion, not electrode passivation by LiF.

To summarize, the initial SEI formed on copper from LP30 electrolyte with 100 ppm added HF consists of crystalline LiF particles with (111) crystallographic texture covered by amorphous solvent reduction products such as organic species and LiOH. It has been reported in literature that grain boundaries between individual crystalline LiF particles and interfaces between LiF and an amorphous phase can act as fast lithium diffusion pathways.[43–45] For example, Zhang *et al.* showed that the interface between crystalline LiF and amorphous Li_2CO_3 can create enhanced lithium-ion diffusivity. For our case, the areal density of these fast diffusion pathways is determined by the number density of LiF particles on the copper surface, which we hypothesize is controlled by the HF concentration and cycling rate, allowing for the direct tuning of SEI properties via electrolyte additive engineering and formation cycling protocols. Such

control over the initial SEI allows for control of initial lithium metal nucleation and growth and the ability to direct a desired lithium morphology.

Crystallographic Texturing of Lithium Columns

In situ GIWAXS was again employed to probe the crystallinity and texturing of electrodeposited lithium metal in electrolytes with and without added HF. While lithium deposited by galvanostatic cycling at 0.5 mA/cm^2 to a capacity of 1 mAh/cm^2 in as-received LP30 electrolyte does not exhibit any preferred texture (Figure S6), lithium deposited in LP30 with 100 ppm added HF has a strong (110) crystallographic texture as evidenced by the peaks at ±60° in the I(χ) analysis (Figure 10b). Shi *et al.* have also reported lithium metal with a (110) texture, though in a different electrolyte system.[46] This (110) texture can be explained by the fact that lithium is a body centered cubic metal, with the close packed crystallographic plane being the (110). However, DFT has shown the lithium (100) plane to have the lowest energy[47,48], although these DFT calculations are for surface energies in vacuum. Electrodeposition is inherently in liquid electrolyte, where both diffusion of lithium ions in the bulk electrolyte and the SEI play critical roles in determining lithium deposit morphology, and this may lead to a (110) texturing.[46,49]

Li *et al.* used cryogenic transmission electron microscopy to show that lithium whiskers are single crystalline, even in electrolytes without additives.[50] In electrolytes that do not produce an aligned columnar microstructure, these individual whiskers bend at random orientations, disrupting any relative coherence between the lithium whiskers and the substrate, as well as between individual lithium whiskers, resulting in a mossy microstructure devoid of texture. However, in electrolytes with added HF, we propose the initial LiF-nanostructured SEI with uniformly high lithium diffusivity promotes a fast nucleation event with high nucleation density; ~70 nuclei/μm^2 at 0.5 mA/cm^2 in this work compared to ~0.5 nuclei/μm^2 reported in reference [51] without HF added. A similar positive correlation between uniformity of SEI properties and high nucleation density was observed by Meyerson *et. al* for nucleation on lithium metal foils.[52] Nucleation is followed by simultaneous lateral and vertical growth of lithium deposits until they bump into one another laterally, leaving the only available growth direction as the one normal to the copper substrate. The uniformity of growth is enabled by high lithium-ion diffusion within the SEI, allowing lithium ions to easily move laterally across the electrode surface thus eliminating sites of preferential deposition which can lead to mossy microstructures. Growth from this point on is along the vertical direction, resulting in a highly monodispersed columnar geometry.

As seen in the XPS spectra in Figure 11, the SEI on lithium deposited by galvanostatic cycling at 0.5 mA/cm^2 to a capacity of 1 mAh/cm^2 in LP30 with 100 ppm added HF is thin enough to allow for detection of Li^0 signal after only 1 minute of sputtering, while no Li^0 is detectable for the SEI formed in as-received LP30 even after 20 minutes of sputtering at the same rate. The lack of Li^0 signal in the SEI formed in as-received electrolyte may be due both to a thicker SEI as well as the effect of the mossy morphology on Ar ion sputtering uniformity. We infer that the higher lithium diffusivity of the SEI formed in electrolyte with added HF enables a more uniform microstructure of the lithium metal with lower surface area and reduces the extent

of continuous electrolyte reduction, resulting in a thinner SEI. The initial simultaneous lateral and vertical growth of lithium metal followed by unidirectional, vertical growth normal to the substrate is aided by this thinner SEI. Depth profiling of the SEI on 1 mAh/cm^2 of electrodeposited lithium formed in HF containing electrolyte reveals a bilayer-like structure with a LiF-rich outer layer and Li_2O-rich inner layer (Figure S7), which is consistent with that reported by Kanamura *et al*.[18] Li_2C_2 has been reported to form alongside Li_2O as a product of carbonate decomposition, which is further supported by the results presented here.[53]

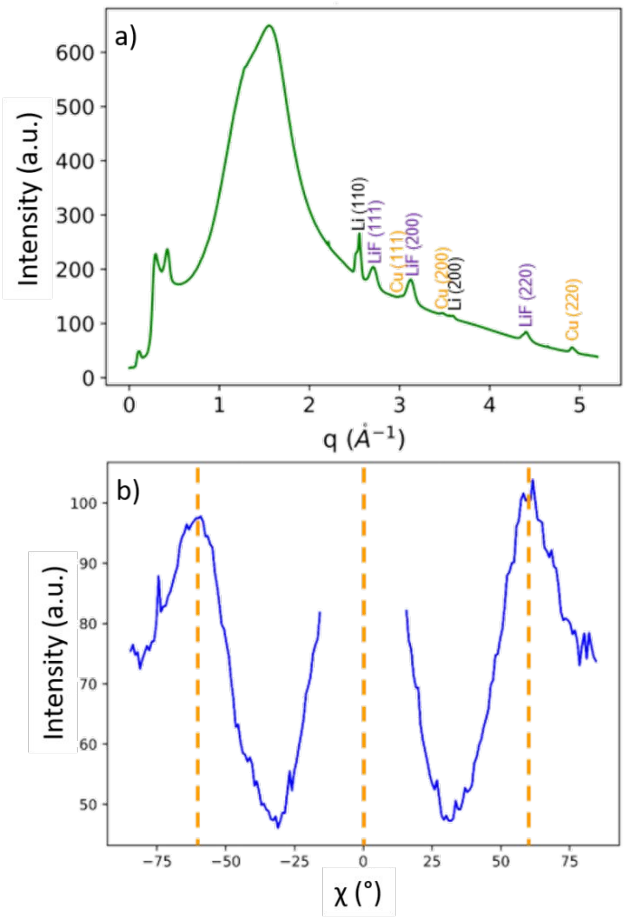

Figure 10: (a) 1D scattering pattern of SEI formed on electrodeposited lithium metal in LP30 with 100 ppm added HF by galvanostatic cycling at 0.5 mA/cm^2 to a capacity of 1 mAh/cm^2. The large broad peak around 1.5 Å^{-1} is due to amorphous scattering from the liquid electrolyte and glass substrate. (b) I(χ) analysis at the Li (110) diffraction peak showing peaks at ± 60° (dashed lines) indicative of (110) texturing.

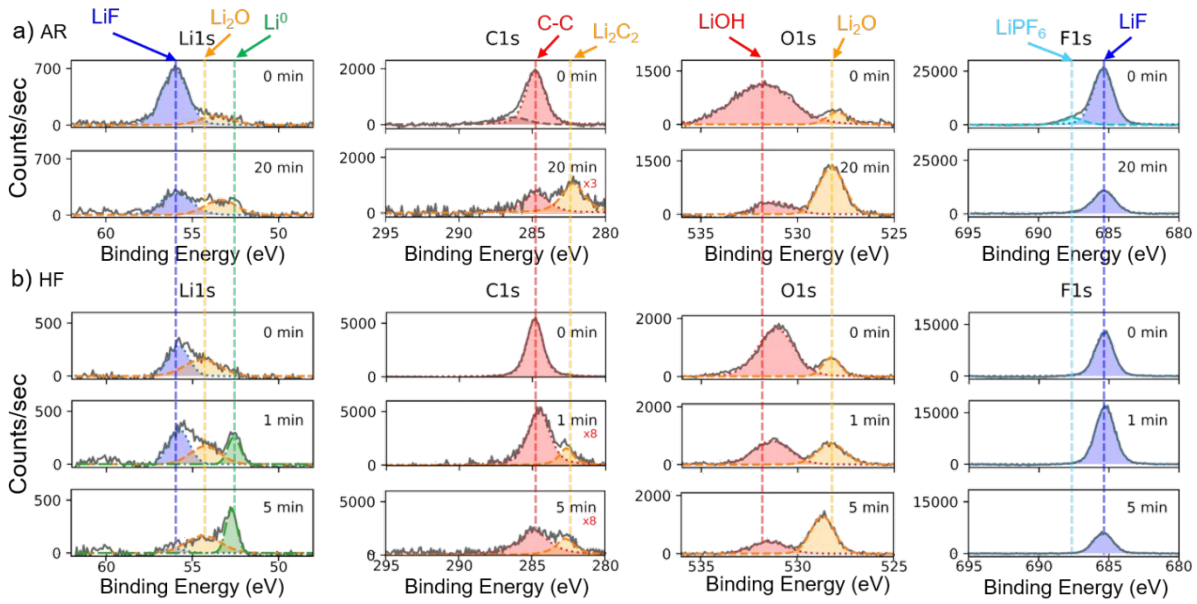

Figure 11: (a) XPS depth profiling spectra of SEI on electrodeposited lithium metal in as-received LP30. (b) XPS spectra of SEI on lithium metal in LP30 with 100 ppm added HF. Times indicate extent of argon ion sputtering.

Persistence of Columnar Morphology After Cycling

To test the cyclability of columnar lithium metal during cell operation, *operando* GISAXS was used to probe the morphology of lithium metal deposits during cycling. GISAXS, being sensitive to length scales on the order of a few to a few hundred nanometers, exhibits a distinct set of evenly spaced intensity oscillations in the q_y direction (Figure 12) arising from the highly monodispersed columnar microstructure, with column diameters of ~100-200 nm depending on current density (Figure S8); the periodicity Δq_y of these oscillations is related to the column diameter d by $\Delta q_y = 2\pi/d$. Oscillations in the q_z direction arise from interference between X-rays scattered from the lithium-electrolyte and lithium-copper interfaces, complicated by multiple scattering and indicate the top surface of the film is very smooth.[54] At the end of plating 1 mAh/cm^2 of lithium, strong intensity oscillations are apparent in the q_y direction, indicative of a columnar morphology (Figure 12c). After stripping half of the plated capacity (0.5 mAh/cm^2), the intensity oscillations are still present, though broader and less pronounced, indicating the columnar morphology is maintained but is less monodisperse in size and shape (Figure 12d). At the end of the second plating half cycle the oscillations are even less pronounced (Figure 12e), suggesting that cycling a large percentage of the plated 1 mAh/cm^2 capacity, in this case 50%, with a columnar morphology leads to a loss of uniformity in the microstructure. This is further evidenced by the fact that if all the columnar lithium is stripped to a 1 V vs Li/Li$^+$ cutoff voltage, the second plating half cycle does not produce a columnar morphology (Figure S9). This is consistent with the report from Zhang *et al*. which demonstrated using *ex situ* SEM that lithium is stripped from both the tops and sides of lithium nanorods[26], enabled by the high lithium-ion diffusivity of the SEI, disrupting uniform re-plating onto the high aspect ratio columns. This limits the cycle life of practical batteries which must

uniformly plate and strip high capacities of lithium during each charge/discharge cycle, particularly in "anode-free" configurations. Thus, further understanding the impact of additional conditions, including electrochemical profile and mechanical compression (stack pressure), which could help promote the growth of columns with a lower aspect ratio (disc-like rather than rod-like), will be crucial to maintaining morphology control after hundreds of cycles and enhancing the long term cyclability of lithium metal batteries. The effects of compression, the presence of a separator, and lower volume of electrolyte, in particular, require additional investigation as the behavior observed using the flooded open cell design employed in this study may not be directly transferable to a commercial-type battery.

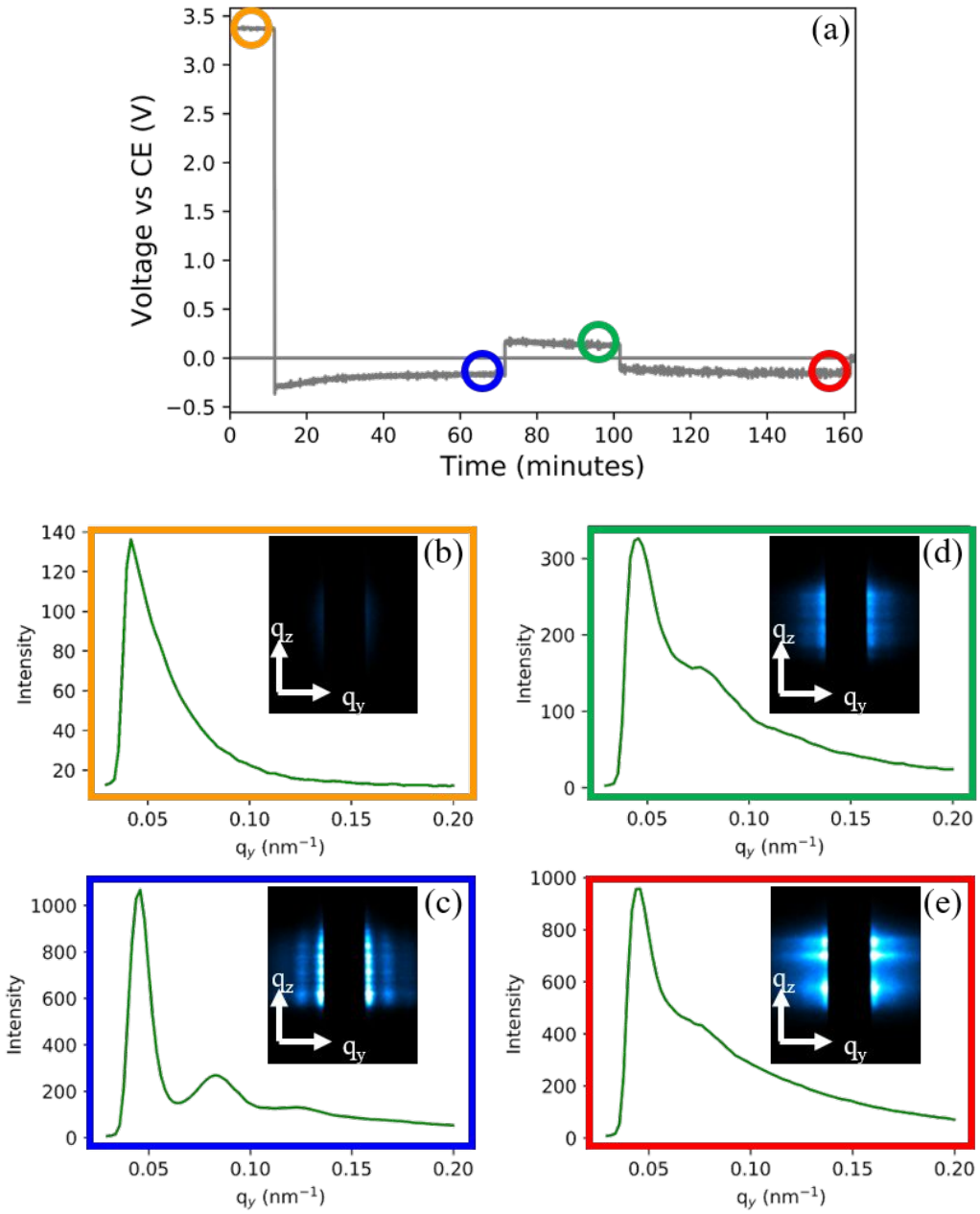

Figure 12: (a) Voltage profile over time for the first plating, partial stripping, and second plating half cycles of lithium on copper in LP30 electrolyte with 100 ppm added HF cycled at a constant current of 1.0 mA/cm^2. (b-e) 1D GISAXS Intensity vs q_y profiles from the timepoints indicated, where intensity oscillations show evidence for the presence of a columnar morphology. Insets show the raw 2D detector images.

Proposed Mechanism of Columnar Lithium Metal Deposition

Combining the insights derived from the systematic set of experiments detailed in this report along with complimentary results from literature, we have uncovered a new understanding of the mechanisms underlying the growth of columnar lithium metal. A schematic representation

of the proposed mechanism linking electrolyte additive concentration, initial SEI formation, and the resulting growth of lithium columns is shown in Figure 13. The initially pristine, oxide-free copper surface enables the electrocatalytic reduction of HF at ~2 V vs Li/Li^+ which forms (111) textured LiF deposits a few nanometers in size on the surface. Two morphologically distinct yet functionally equivalent LiF deposit morphologies are possible – uniform yet discontinuous LiF particles decorating the copper surface or a continuous polycrystalline film - with the former being more probable in this system when considering the substrate roughness and LiF crystallite size. This HF reduction and LiF deposition process slows significantly when HF becomes depleted near the interface. Subsequently, as the potential drops below 1 V, solvent molecules are decomposed on the remaining unpassivated surfaces between and/or on top of LiF particles, forming organic reduction products and slowing further reduction of electrolyte species. While the precise morphology of the LiF particle layer could not be directly imaged, both candidate morphologies shown schematically in Figure 13 would result in an SEI with similar properties and identical effects on lithium nucleation and growth. Interfaces between individual crystalline LiF particles and/or between LiF particles and the amorphous matrix of solvent reduction products in the initial SEI act as fast lithium-ion diffusion pathways. These pathways serve to homogenize the electronic and ionic properties near the copper surface, enabling a high nucleation density of lithium metal as the potential of the working electrode is brought below 0 V vs Li/Li^+ and electrodeposition of the active material begins via an instantaneous nucleation event. High lithium-ion diffusion within the SEI created by these interfaces, which allows for easier movement of lithium ions laterally across the electrode surface, along with the layer being very thin, allow for uniform, lateral growth of the lithium metal deposits until they bump into one another. After lateral growth is inhibited the deposits are restricted to growing vertically, normal to the working electrode, resulting in the highly monodisperse (110) textured columnar morphology observed. The diameter of these lithium columns can be controlled by varying the current density during electrodeposition (Figure S8). Indeed, a columnar morphology may be the intrinsically preferred growth mode of lithium metal[21,55]. However, such growth may be inhibited by the SEI formed in conventional electrolytes without additives due to non-uniform lithium-ion diffusivity and the presence of "hot spots" where preferential deposition occurs, whereas the nanostructured SEI formed in electrolytes with added HF would allow columnar growth to proceed uninhibited.

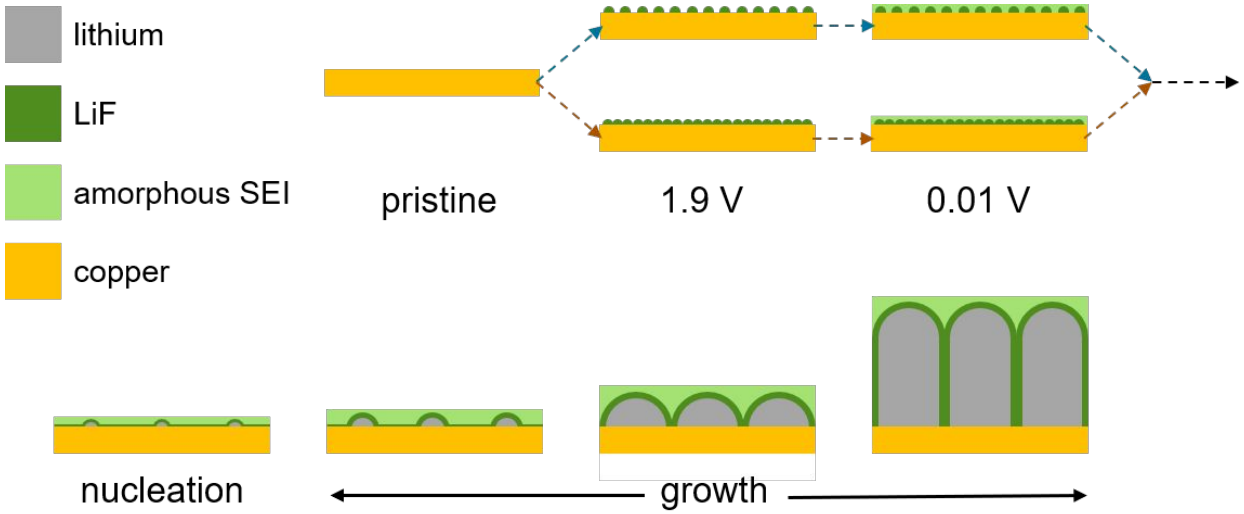

Figure 13: Schematic (cross-sectional view) showing the series of processes resulting in an SEI layer containing crystalline LiF particles in an amorphous matrix which directs the growth of highly monodispersed columns of lithium metal. Crystalline LiF is produced as a product of selective HF reduction at 2 V vs Li/Li$^+$, followed by solvent reduction at lower potentials yielding amorphous products. The high lithium diffusivity of the nanostructured SEI promotes high lithium nucleation density, and allows for uniform lateral growth, and eventually the formation of a columnar morphology.

Conclusions

In this work, a mechanism is proposed to explain the phenomenon of columnar lithium metal deposition. An electrolyte additive, such as HF, is selectively reduced at high potential vs Li/Li$^+$ to form uniformly distributed crystalline LiF particles with preferred crystallographic texture which are then encased in an amorphous matrix of solvent reduction products, as evidenced by systematic electrochemical analysis and *in situ* X-ray surface scattering. The LiF quantity and distribution are directly tunable by choosing an appropriate additive concentration and electrochemical cycling rate. Interfaces between LiF and the amorphous phase act as fast lithium-ion diffusion pathways, promoting a thin and more uniform SEI which leads to a very high lithium metal nucleation density relative to additive-free systems followed by nearly-isotropic and eventually vertical columnar growth, observed in real-time using *operando* small angle X-ray scattering. Understanding this process step-by-step provides new insights into the role of electrolyte additives and provides new information for the rational design of such additives. As HF is damaging to cathodes, current collectors, and other cell components, new additives which decompose at high potentials vs lithium and direct the formation of a columnar morphology should be developed for practical use in lithium metal batteries.

Conflicts of Interest

The authors have no conflicts of interest to declare.

Acknowledgements

The authors acknowledge support from the Assistant Secretary for Energy Efficiency and Renewable Energy, Office of Vehicle Technologies of the U.S. Department of Energy under the

Battery 500 Consortium. Use of the Stanford Synchrotron Radiation Lightsource (SSRL), SLAC National Accelerator Laboratory, is supported by the U.S. Department of Energy, Office of Science, Office of Basic Energy Sciences under Contract No. DE-AC02-76SF00515. Part of this work was performed at the Stanford Nano Shared Facilities (SNSF), supported by the National Science Foundation under award ECCS-1542152. N. R. Geise acknowledges support by the US Department of Defense through the National Defense Science & Engineering Graduate Fellowship (NDSEG) Program. The authors thank Nicholas Melosh for use of his group's SEM.

References

1 R. Cao, W. Xu, D. Lv, J. Xiao and J.-G. Zhang, *Adv. Energy Mater.*, 2015, **5**, 1–23.

2 X. B. Cheng, R. Zhang, C. Z. Zhao, F. Wei, J. G. Zhang and Q. Zhang, *Adv. Sci.*, 2015, **3**, 1–20.

3 K. N. Wood, E. Kazyak, A. F. Chadwick, K. H. Chen, J. G. Zhang, K. Thornton and N. P. Dasgupta, *ACS Cent. Sci.*, 2016, **2**, 790–801.

4 B. D. Adams, J. Zheng, X. Ren, W. Xu and J. G. Zhang, *Adv. Energy Mater.*, 2018, **8**, 1–11.

5 Y. Li, Y. Li, Y. Sun, B. Butz, K. Yan, A. L. Koh, J. Zhao, A. Pei and Y. Cui, *Nano Lett.*, 2017, **17**, 5171–5178.

6 L. F. Nazar, M. Cuisinier and Q. Pang, *MRS Bull.*, 2014, **39**, 436–442.

7 G. Crabtree, *AIP Conf. Proc.*, 2015, **1652**, 112–128.

8 D. Lin, Y. Liu and Y. Cui, *Nat. Nanotechnol.*, 2017, **12**, 194–206.

9 P. Bai, J. Li, F. R. Brushett and M. Z. Bazant, *Energy Environ. Sci.*, 2016, **9**, 3221–3229.

10 K. N. Wood, M. Noked and N. P. Dasgupta, *ACS Energy Lett.*, 2017, **2**, 664–672.

11 H. J. Chang, N. M. Trease, A. J. Ilott, D. Zeng, L. S. Du, A. Jerschow and C. P. Grey, *J. Phys. Chem. C*, 2015, **119**, 16443–16451.

12 B. Wu, J. Lochala, T. Taverne and J. Xiao, *Nano Energy*, 2017, **40**, 34–41.

13 R. D. Rauh and S. B. Brummer, *Electrochim. Acta*, 1977, **22**, 75–83.

14 J. Lopez, A. Pei, J. Y. Oh, G. J. N. Wang, Y. Cui and Z. Bao, *J. Am. Chem. Soc.*, 2018, **140**, 11735–11744.

15 B. Liu, J. G. Zhang and W. Xu, *Joule*, 2018, **2**, 833–845.

16 N. Singh, T. S. Arthur, M. Jones, O. Tutusaus, K. Takechi, T. Matsunaga, R. Kerr, P. C. Howlett, M. Forsyth and F. Mizuno, *ACS Appl. Energy Mater.*, 2019, **2**, 8912–8918.

17 J. Liu, Z. Bao, Y. Cui, E. J. Dufek, J. B. Goodenough, P. Khalifah, Q. Li, B. Y. Liaw, P. Liu, A. Manthiram, Y. S. Meng, V. R. Subramanian, M. F. Toney, V. V. Viswanathan, M. S. Whittingham, J. Xiao, W. Xu, J. Yang, X. Q. Yang and J. G. Zhang, *Nat. Energy*, 2019, **4**, 180–186.

18 K. Kanamura, S. Shiraishi and Z. I. Takehara, *J. Electrochem. Soc.*, 1994, **141**, L108–L110.

19 J. Qian, W. Xu, P. Bhattacharya, M. Engelhard, W. A. Henderson, Y. Zhang and J. G. Zhang, *Nano Energy*, 2015, **15**, 135–144.

20 W. Chang, J. H. Park and D. A. Steingart, *Nano Lett.*, 2018, **18**, 7066–7074.

21 W. Chang, J. H. Park, N. S. Dutta, C. B. Arnold and D. A. Steingart, *Chem. Mater.*, 2020, **32**, 2803–2814.

22 S. F. Lux, I. T. Lucas, E. Pollak, S. Passerini, M. Winter and R. Kostecki, *Electrochem. commun.*, 2012, **14**, 47–50.

23 D. Strmcnik, I. E. Castelli, J. G. Connell, D. Haering, M. Zorko, P. Martins, P. P. Lopes, B. Genorio, T. Østergaard, H. A. Gasteiger, F. Maglia, B. K. Antonopoulos, V. R. Stamenkovic, J. Rossmeisl and N. M. Markovic, *Nat. Catal.*, 2018, **1**, 255–262.

24 D. Aurbach, M. Moshkovich, Y. Cohen and A. Schechter, *Langmuir*, 1999, **15**, 2947–2960.

25 O. Borodin, X. Ren, J. Vatamanu, A. Von Wald Cresce, J. Knap and K. Xu, *Acc. Chem. Res.*, 2017, **50**, 2886–2894.

26 Y. Zhang, J. Qian, W. Xu, S. M. Russell, X. Chen, E. Nasybulin, P. Bhattacharya, M. H. Engelhard, D. Mei, R. Cao, F. Ding, A. V. Cresce, K. Xu and J. G. Zhang, *Nano Lett.*, 2014, **14**, 6889–6896.

27 X. Ren, Y. Zhang, M. H. Engelhard, Q. Li, J. G. Zhang and W. Xu, *ACS Energy Lett.*, 2018, **3**, 14–19.

28 X. Q. Zhang, X. Chen, R. Xu, X. B. Cheng, H. J. Peng, R. Zhang, J. Q. Huang and Q. Zhang, *Angew. Chemie - Int. Ed.*, 2017, **56**, 14207–14211.

29 J. Qian, B. D. Adams, J. Zheng, W. Xu, W. A. Henderson, J. Wang, M. E. Bowden, S. Xu, J. Hu and J. G. Zhang, *Adv. Funct. Mater.*, 2016, **26**, 7094–7102.

30 M. Genovese, A. J. Louli, R. Weber, S. Hames and J. R. Dahn, *J. Electrochem. Soc.*, 2018, **165**, A3321–A3325.

31 Y. W. Chen, J. D. Prange, S. Dühnen, Y. Park, M. Gunji, C. E. D. Chidsey and P. C. McIntyre, *Nat. Mater.*, 2011, **10**, 539–544.

32 A. J. Bard and L. R. Faulkner, *Electrochemical Methods: Fundamentals and Applications*, John Wiley & Sons, Inc., 2nd edn., 2001.

33 C. Cao, H. Steinrück, B. Shyam and M. F. Toney, 2017, **1700771**, 1–7.

34 H. Steinrück, C. Cao, G. M. Veith and M. F. Toney, *J. Chem. Phys.*, 2020, **152**, 084702.

35 G. Ashiotis, A. Deschildre, Z. Nawaz, J. P. Wright, D. Karkoulis, F. E. Picca and J. Kieffer, *J. Appl. Crystallogr.*, 2015, **48**, 510–519.

36 T. Dane, https://github.com/tgdane/pygix.

37 W. Huang, D. T. Boyle, Y. Li, Y. Li, A. Pei, H. Chen and Y. Cui, *ACS Nano*, 2019, **13**, 737–744.

38 H. Zhang, G. G. Eshetu, X. Judez, C. Li, L. M. Rodriguez-Martínez and M. Armand, *Angew. Chemie - Int. Ed.*, 2018, **57**, 15002–15027.

39 P. Novak, F. Joho, M. Lanz, B. Rykart, J. Panitz, O. Haas and D. Alliata, 2001, **98**, 39–46.

40 K. Leung, 2015, 1637–1643.

41 C. Cao, T. P. Pollard, O. Borodin, J. E. Mars, C. J. Takacs, Y. Tsao, M. Lukatskaya, M. Schroeder, K. Xu, M. F. Toney and H.-G. Steinrück, *Prep.*

42 N. P. W. Langenhuizen, *J. Electrochem. Soc.*, 1998, **145**, 3094.

43 Q. Zhang, J. Pan, P. Lu, Z. Liu, M. W. Verbrugge, B. W. Sheldon, Y. T. Cheng, Y. Qi and X. Xiao, *Nano Lett.*, 2016, **16**, 2011–2016.

44 Y. Li, W. Huang, Y. Li, A. Pei, D. T. Boyle and Y. Cui, *Joule*, 2018, **2**, 2167–2177.

45 R. Xu, C. Yan, Y. Xiao, M. Zhao, H. Yuan and J. Q. Huang, *Energy Storage Mater.*, , DOI:10.1016/j.ensm.2019.12.020.

46 F. Shi, A. Pei, A. Vailionis, J. Xie, B. Liu, J. Zhao, Y. Gong and Y. Cui, *Proc. Natl. Acad. Sci. U. S. A.*, 2017, **114**, 12138–12143.

47 K. Doll, N. M. Harrison and V. R. Saunders, *J. Phys. Condens. Matter*, 1999, **11**, 5007–5019.

48 R. Tran, Z. Xu, B. Radhakrishnan, D. Winston, W. Sun, K. A. Persson and S. P. Ong, *Sci. Data*, 2016, **3**, 321–325.

49 P. Biswal, S. Stalin, A. Kludze, S. Choudhury and L. A. Archer, *Nano Lett.*, , DOI:10.1021/acs.nanolett.9b03548.

50 Y. Li, Y. Li, A. Pei, K. Yan, Y. Sun, C. L. Wu, L. M. Joubert, R. Chin, A. L. Koh, Y. Yu, J. Perrino, B. Butz, S. Chu and Y. Cui, *Science (80-.).*, 2017, **358**, 506–510.

51 A. Pei, G. Zheng, F. Shi, Y. Li and Y. Cui, *Nano Lett.*, 2017, **17**, 1132–1139.

52 M. L. Meyerson, J. K. Sheavly, A. Dolocan, M. P. Griffin, A. H. Pandit, R. Rodriguez, R. M. Stephens, D. A. Vanden Bout, A. Heller and C. B. Mullins, *J. Mater. Chem. A*, 2019, **7**, 14882–14894.

53 V. Eshkenazi, E. Peled, L. Burstein and D. Golodnitsky, *Solid State Ionics*, 2004, **170**, 83–91.

54 G. Renaud, R. Lazzari and F. Leroy, *Surf. Sci. Rep.*, 2009, **64**, 255–380.

55 J. Steiger, G. Richter, M. Wenk, D. Kramer and R. Mönig, *Electrochem. commun.*, 2015, **50**, 11–14.

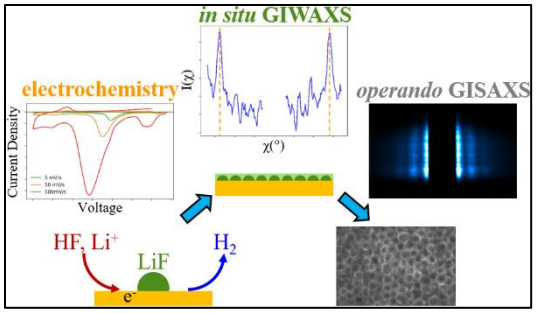

Investigation of the mechanisms underlying control of electrodeposited lithium metal morphology using electrolyte additives in lithium metal batteries.